npj | climate and atmospheric science

Brief communication

Published in partnership with CECCR at King Abdulaziz University

https://doi.org/10.1038/s41612-025-00978-1

# Divergent response of aridity index to historical land use and land cover change



Tao Tang[1,2] ✉, Jun Ge[3], Haiyun Shi[4] & Junji Cao[2] ✉

By using model simulations, we show that historical land use and land cover change since 1850 has impacted aridity index (AI) worldwide, causing divergent responses in different regions. Locally, AI tends to increase (getting humid) in reforestation regions and most humid regions. Owing to these changes, the area of the humid zone expanded insignificantly by 0.22% of the global land area at the expense of drylands.

Aridity index (AI), defined as the ratio of annual precipitation (P) to annual potential evapotranspiration (PET), measures long-term surface dryness and has great implications for the ecological environment and natural systems[1]. An increase in aridity (decreased AI) can cause slowed vegetation growth[2], reduced terrestrial carbon uptake[3], loss of biodiversity[4], weaker vegetation resilience and possible environmental degradation[5], as well as overall modifications of ecosystem functions[6]. The currently reported change in AI is the response of aridity to all the climate forcings combined[7], in which greenhouse gases dominate the response[8]. The impact of historical land use and land cover change (LULCC) alone on aridity is far from clear due to the lack of long-term observations, because it is difficult to separate the LULCC signal from the pure observational records. Besides, many countries are planning reforestation programs to combat climate change and environmental degradation (e.g., Bonn Challenge: https://www.bonnchallenge.org/). The impact of LULCC on aridity, if any (i.e., alleviating aridity), can provide scientific guidance for land-management policy makers. In this brief communication, we report that historical LULCC has significantly modified aridity worldwide.

Two sets of CMIP6 model simulations are employed in this study, one with historical LULCC (hist) from1850 to 2014 and the other with fixed LULCC at the 1850 level (hist-noLu; see methods). The impact of LULCC on AI was quantified as the difference between the two simulations (AI in the hist simulation minus AI in the hist-noLu simulation), denoted as ΔAI. For each simulation, AI was calculated as the ratio of P over PET, in which P and PET are 20-year annual mean values over 1995–2014. The results are shown in multi-model mean (MMM) values, with the same weighting factor assigned to each model. It is noted that the concentrations of atmospheric carbon dioxide are identical in both simulations. Thus, only the biophysical effects related to changes in surface properties (e.g., albedo, aerodynamic roughness and evapotranspiration efficiency) and associated atmospheric feedbacks are considered here.

Historical LULCC between 1850 and 2014 is primarily manifested as the loss of primary and secondary land (psl) and the concomitant expansion of cropland, pasture, and rangeland. During this period, psl decreased by ~21.6% (28.5 $Mkm^2$) of the global land area, including roughly loss of 6.6 $Mkm^2$ forests. At the same time, cropland, pasture, and rangeland expanded by 6.5%, 3.6% and 10.9%, respectively (Fig.S1).

The first question is whether LULCC activity (mainly deforestation) can significantly affect local AI. To answer this question, we binned ΔAI and its two terms as a function of psl fraction changes at an interval of 10% (Fig. 1). It is seen that ΔAI is negligible or slightly negative over most of the deforestation regions, but substantially positive in reforestation regions (Fig. 1a). Based on a linear regression, ΔAI decreases by approximately 0.004 ($r = 0.82$; $p < 0.001$) in response to every 10% loss in the psl fraction. This trend, however, is mainly contributed by positive ΔAI in reforestation regions. A similar relationship is also observed for ΔP, in which ΔP tends to be slightly negative over deforestation regions and substantially positive in reforestation regions (Fig. 1b), with a slope of 0.005 mm $day^{-1}$ ($r = 0.81$; $p < 0.001$) per bin. An opposite change, however, is found for ΔPET, and stronger deforestation activity tends to produce positive ΔPET (Fig. 1c).

When the land grids are divided into deforestation grids (psl fraction change <−5%), reforestation grids (psl fraction change >= 5%) and grids without significant LULCC (psl fraction changes within ±5%), the above reported relationship is more pronounced. On average, deforestation causes an insignificant decrease of 0.002 in AI, whereas reforestation causes an increase of 0.041 in AI (Fig. 1a), with statistical significance at the $p = 0.10$ level. The slight negative ΔAI over deforestation regions is largely attributed to negative ΔP while the positive ΔAI over reforestation regions is driven by both positive ΔP and negative ΔPET. In regions without significant LULCC, AI increases by 0.010. These changes altogether lead to an insignificant increase of 0.004 [ − 0.006 0.031] (MMM value and 90% confidence interval (CI)) in AI globally, which is mainly due to negative ΔPET (purple bars in Fig. 1a, c).

The spatial patterns of ΔAI are shown in Fig. 2a, along with the contributions from ΔP and ΔPET in Fig. 2b, c (see Methods). Significant decreases in AI are largely seen in the lower latitude regions, such as the

[1]National Key Laboratory of Earth System Numerical Modelling and Application, Institute of Atmospheric Physics, Chinese Academy of Sciences, Beijing, 100029, China. [2]Science Center for Earth System Numerical Simulation, Institute of Atmospheric Physics, Chinese Academy of Sciences, Beijing, 100029, China. [3]Joint International Research Laboratory of Atmospheric and Earth System Sciences, School of Atmospheric Sciences, Nanjing University, Nanjing, 210023, China. [4]School of Environmental Science and Engineering, Southern University of Science and Technology, Shenzhen, 518055, China. ✉e-mail: tangtao@mail.iap.ac.cn; jjcao@mail.iap.ac.cn

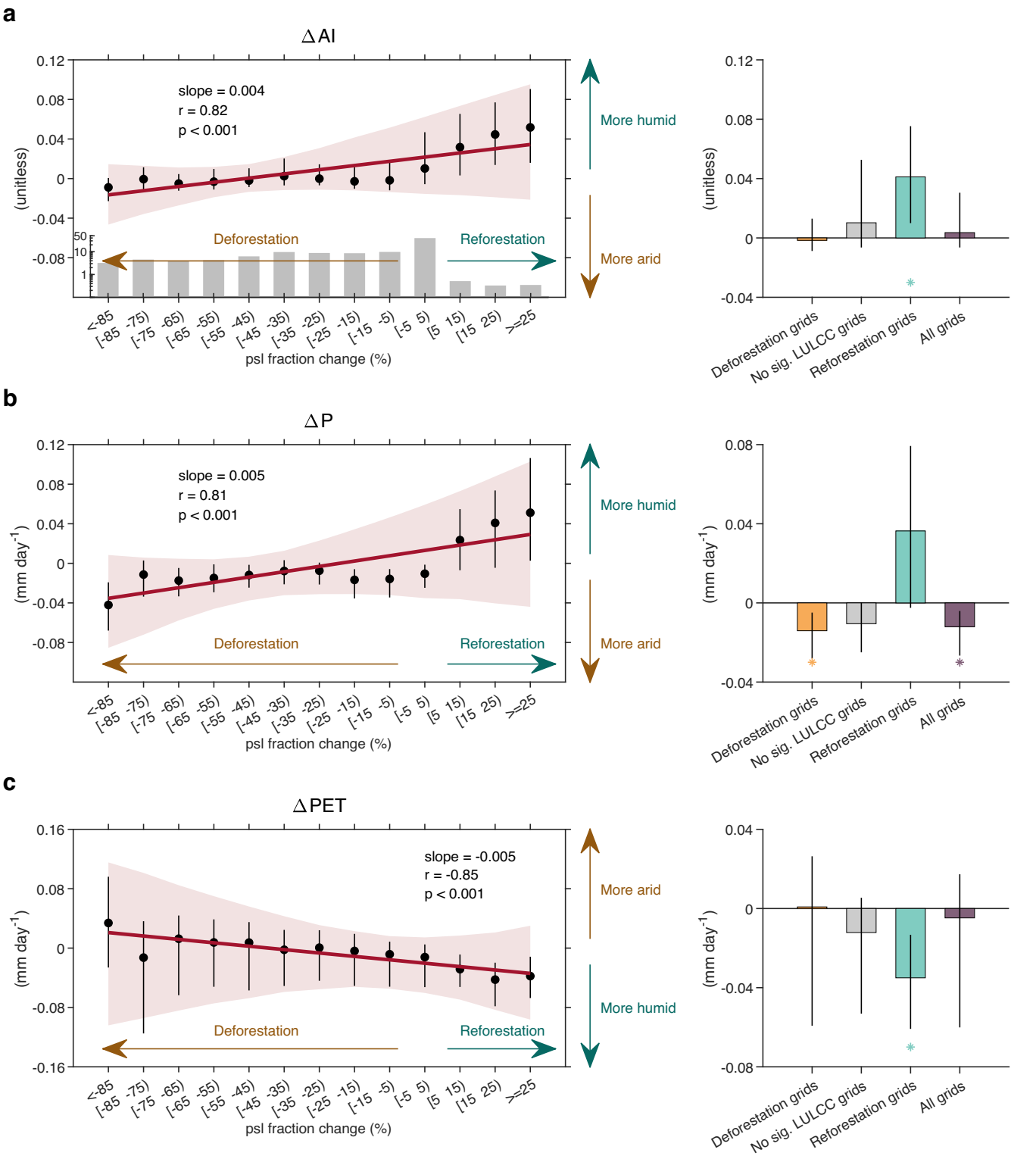


**Fig. 1 | Changes in aridity terms as a function of psl fraction changes.** Changes in AI (**a**), P (**b**), and PET (**c**) binned by the fraction changes in primary and secondary land (psl) at intervals of 10%. Negative (positive) psl fraction changes denote deforestation (reforestation). Black dots denote the MMM values of each bin, and vertical lines denote the 90% confidence interval (CI) of each bin. The red lines are least-square linear regressions based on the MMM values of each bin, along with the slope and correlation coefficient values (*r*) being shown. The red shaded regions are the 90% regression estimates based on a bootstrap technique. The inserted gray bar plot in (a) shows the land fractions of each bin relative to the global land (without Antarctica and Greenland) on a logarithmic scale. The bar plots in each panel are the corresponding terms averaged over the deforestation grids, reforestation grids, grids without significant LULCC and all grids.

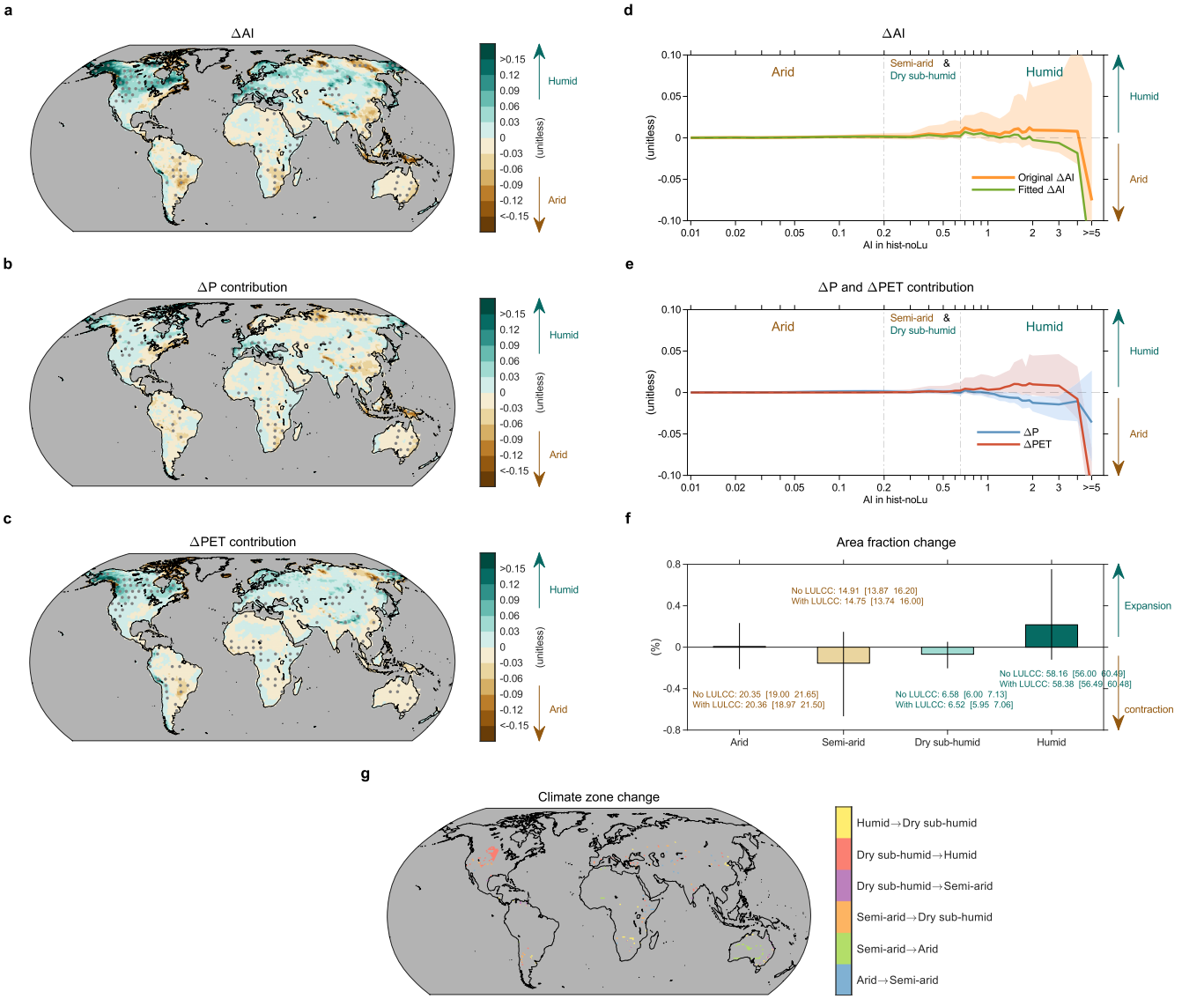


**Fig. 2 | Changes in aridity terms and climate zones.** Spatial pattern of multi-model mean (MMM) changes in aridity index (AI) (**a**), contributions by ΔP (**b**), and contributions by ΔPET (**c**). **d** MMM changes of original PET and fitted PET as a function of the background AI. **e** MMM values of contributions from ΔP and ΔPET as a function of background AI. **f** Area fraction changes in the four climate zones due to LULCC. **g** Spatial pattern of climate zone shifts. In (a-c), gray dots indicate that the changes and contributions are statistically significant at the $p = 0.10$ level, which are shown every 5 rows and columns for clarity. In (d) and (e), solid lines denote MMM values of the 11 models, and the shading denotes the 90% confidence interval (CI). In (f), bars denote MMM values and error bars denote the 90% CI. All percentage values in (f) are area fractions relative to the global land without Antarctica and Greenland. The area fractions of each climate zone with and without LULCC are also listed in (f) in the MMM value and 90% CI.

Amazon, Indonesia and Australia, whereas significant increases in AI are mainly observed in the mid-to-high latitude regions, especially North America and Europe. This pattern is different from those caused by GHGs, aerosols and natural forcings[8], implying a distinct response of surface water and energy fluxes due to LULCC. Further analysis indicates that the spatial pattern of ΔPET is largely driven by changes in temperature and vapor pressure deficit (Fig. S3). These two variables combined can explain approximately 72% of the spatial variability in ΔPET. When aggregating ΔAI by background AI (AI value in the hist-noLu simulation), it is seen that ΔAI is negligible in most drylands (AI < 0.65) and positive in humid regions where AI < 4 (Fig. 2d). The positive ΔAI in humid regions is contributed by ΔPET and partially offset by ΔP (Fig. 2e). In regions with AI > 4, however, ΔAI is negative, which is contributed by both ΔP and ΔPET.

In order to better understand how AI responds to LULCC, we further examined the ΔAI on a regional scale based on the IPCC-defined regions (Fig. S4). Of all the 27 land regions, 14 regions show negative ΔAI while the remaining 13 regions show positive ΔAI. Statistically significant drying is seen in Australia, South Africa, and Southeast Asia and significant wetting is found in West North America, Mediterranean, and Central Europe. A closer examination on the LULCC and ΔAI reveals three interesting phenomena. First, a stronger LULCC does not necessarily lead to larger ΔAI. For example, Central Asia (CAS) has the second largest of LULCC in history, but ΔAI shows negligible changes and the opposite is found for Alaska (ALA), where ΔAI shows substantial changes only with limited LULCC. These results imply that nonlocal effects arising from changes in circulation and background climate are crucial in some regions. In other words, AI in a region is affected not only by local LULCC activity, but may also by remote LULCC activity. Second, psl loss can cause both positive and negative ΔAI, which may partially explain the limited responses of AI in deforestation grids (Fig. 1a), as the positive and negative changes are cancelled out.

Third, ΔP and ΔPET play different roles in modifying regional AI. For example, in West North America, ΔAI is mainly contributed by ΔPET whereas in the Amazon, ΔP is dominating. In regions like Tibetan Plateau and North Europe, the contributions of ΔP and ΔPET are opposite.

Global land can be categorized into four different climate zones, including the arid (AI < 0.2), semi-arid (0.2 ≤ AI < 0.5), dry sub-humid (0.5 ≤ AI < 0.65) and humid (AI ≥ 0.65) regions, based on AI. As AI has changed significantly worldwide, the last question is whether LULCC-induced changes in AI further influence the area fraction of the climate zones. Figure 2f shows the area fraction changes in the four climate zones due to historical LULCC. All values in Fig. 2f are area fractions relative to the global land without Antarctica and Greenland (132 $Mkm^2$). Though not statistically significant, the area of the humid region increased by 0.22% of the global land area (mainly in Central North America, Fig. 2g), equivalent to 0.3 $Mkm^2$, at the expense of semi-arid and dry sub-humid zones (largely in Australia). The area fractions of the latter two zones decreased by 0.16% and 0.06%, respectively. When combined, the drylands (a combination of arid, semi-arid and dry sub-humid zones) show a contraction of 0.22% due to LULCC, counteracting the observed expansion trend of drylands under a warming climate reported in previous studies[9]. This also indicates that the observed dryland expansion is largely driven by GHGs and aerosols and then slightly offset by LULCC.

The above analyses reveal that AI tends to increase in reforestation regions, indicating that reforestation has the potential to alleviate local aridity. However, cautions are needed to be taken, as historical reforestation is restricted to a small part of Europe (Fig. S1a). It is not known whether the increase of AI in this region is due to local reforestation or due to changes of circulation and background climate arising from remote LULCC activity[10]. Besides, even if the increased AI in Europe is caused by local reforestation activity, it is not known whether the conclusion drawn in Europe is applicable to other regions considering that the LULCC impact is highly location-dependent[11–13]. Therefore, whether reforestation could alleviate local aridity merits future investigations.

## Materials and methods

### CMIP6 model output

Eleven models (one realization per model) participating in the CMIP6 projects[14] are employed in this study. For each model, two experiments are used to quantify the impact of historical LULCC. The first experiment is the standard historical simulation that includes all anthropogenic forcings (e.g., greenhouse gases, aerosols and LULCC) and natural forcings (e.g., solar and volcanic forcings). The second is the hist-noLu simulation, in which all forcings are identical to those in the historical experiment but with land use fixed at the 1850 level[15]. The LULCC data in all CMIP6 models are prescribed by the Land-Use Harmonization dataset[16]. Both simulations were run in fully coupled mode from 1850 to 2014, and the period of 1995–2014 is chosen for analyses in this study. The detailed information of each model is listed in Table S1. It is noted that the atmospheric concentrations of greenhouse gases in both experiments are identical and are not influenced by historical LULCC. Differences between the two experiments are the biophysical effects of LULCC only. It is worthing noting that, compared with satellite-based studies using the "space-for-time" strategy, which includes direct effects only, our results accounted for the indirect effects arising from the changes in feedbacks and background climate.

### Model performance evaluation

To evaluate the performance of LULCC-induced signal from the model simulations, we compared P, PET, and P/PET from the hist simulation against CRUTS4 data[17]. The comparison was performed based on 20-year annual mean values over 1995-2014 from observational records and the CMIP6 output (Fig. S5). In general, the models can reproduce the observed climatology reasonably well for both P and PET, with the correlation coefficients ($r$) between the MMM values and observational values being 0.83 (P) and 0.96 (PET). For P/PET, the $r$ value between the MMM and CRUTS4 data is 0.64, which is a little bit lower than P and PET. However, the models still reproduced the spatial pattern of climate zones reasonably good (Fig. S5g, h). Given this evaluation outcome, it is suitable to utilize these models in our analyses. We also acknowledge that discrepancies exist over the transition zones, such as Central and West North America and West and Central Asia.

### Calculation of the aridity index

Aridity index is calculated as the ratio of 20-year mean P over PET, in which P is precipitation and PET is the potential evapotranspiration. The latter is the maximum evapotranspiration given unlimited water, which is estimated by the Food and Agricultural Organization Penman–Monteith method[18]:

$$PET = \frac{0.408\Delta\left(R_n - G\right) + \gamma \frac{900}{T+273} u\left(e_s - e_a\right)}{\Delta + \gamma(1 + 0.34u)} \quad (1)$$

where $PET$ is in mm $day^{-1}$, $\Delta$ is the slope of the vapor pressure curve (kPa $°C^{-1}$), $R_n$ is the surface net radiation (MJ $m^{-1}$ $day^{-1}$), $G$ is the soil heat flux (MJ $m^{-1}$ $day^{-1}$), $\gamma$ is the psychometric constant (kPa $°C^{-1}$), $T$ is the 2 m air temperature (°C), $u$ is the surface wind speed (m $s^{-1}$), $e_s$ is the near-surface saturation vapor pressure (kPa), and $e_a$ is the actual vapor pressure (kPa). After estimation of the aridity (AI), the climate zones are defined as arid (AI < 0.2), semi-arid (0.2 ≤ AI < 0.5), dry sub-humid (0.5 ≤ AI < 0.65) and humid (AI ≥ 0.65).

### Quantification of LULCC impact

The LULCC impact, denoted as Δ or change, was quantified as differences in the same variables between the two simulations in each model. Taking precipitation (P) as an example, the impact of LULCC on P is defined as:

$$\Delta P = \overline{P_{hist}} - \overline{P_{hist-noLu}} \quad (2)$$

In Equation [2], Δ is the change in P due to LULCC impact, and the overbars represent the annual mean value of 1995-2014. The changes in PET and AI were estimated similarly by replacing P in Equation [2] with the corresponding variables.

These differences were computed for each grid cell in each model and then averaged to obtain the multi-model mean (MMM) values, with an equal weighting factor assigned to each model. All model outputs were resampled to a common spatial resolution of 0.94° × 1.25° in latitude and longitude before data processing. The re-sampling process was carried out by using a bilinear interpolation.

### Significance test and confidence interval

A bootstrap technique was used to test whether the MMM values are significantly different from zero at the grid-cell level. The 11 model values were sampled 11 times randomly with replacement to obtain a mean value. The process was repeated 1000 times to construct a 90% confidence interval (CI). The MMM changes are considered significant if zero falls outside the confidence interval. Confidence interval was estimated similarly. After obtaining the 1000 mean values, the 5th and 95th percentile values were considered as the 90% confidence interval.

### Regression of changes in AI against LULCC activity

To evaluate the relationship between ΔAI and LULCC activity, as shown in Fig. 1, a linear regression relationship was established. By taking the area-weighted mean value, we binned the changes in AI of all land grids based on the fraction changes in primary and secondary land (psl) with an interval of 10% for each model. Thus, there are 11 values for each bin and 13 bins in total. A linear regression model was subsequently constructed based on the MMM values in each bin. The uncertainty range of the regression was estimated with a bootstrap technique. Specifically, we randomly sampled the 11 data points in each bin and obtained 13 randomly sampled data points in total to construct a linear regression model. This process was repeated 1000 times to obtain the 90% CI (gray shaded region of the regression in Fig. 1).

### Decomposition of ΔAI

By using Taylor Series, ΔAI could be approximated as the summation of two terms:

$$\Delta AI \approx \frac{\Delta P}{P_{hist-noLu}} AI_{hist-noLu} - \frac{\Delta PET}{PET_{hist-noLu}} AI_{hist-noLu} \quad (3)$$

On the right-hand side of Equation [3], ΔP and ΔPET represent the P and PET changes (hist minus hist-noLu) estimated from Equation [2]. $P_{hist-noLu}$, $PET_{hist-noLu}$, and $AI_{hist-noLu}$ denote P, PET and AI, respectively, in the hist-noLu simulations. The first term of the right-hand side is therefore the change in AI attributed to ΔP, and the second term of the right-hand side is the change in AI attributed to ΔPET.

## Data availability

All data in this study are freely available from the web: The CMIP6 data was collected from the Earth System Grid Federation (ESGF) portal at https://esgf-node.llnl.gov/projects/cmip6/; The P and PET data were collected from https://crudata.uea.ac.uk/cru/data/hrg/cru_ts_4.04/cruts.2004151855.v4.04/. LULCC data is downloaded from https://luh.umd.edu/.

## Code availability

The MATLAB scripts used for processing the data are available upon reasonable request from the corresponding author

Received: 20 December 2024; Accepted: 20 February 2025;
Published online: 05 March 2025

## References

1. Berdugo, M. et al. Global ecosystem thresholds driven by aridity. *Science* **367**, 787–790 (2020).
2. Williams, A. P. et al. Forest responses to increasing aridity and warmth in the southwestern United States. *Proc. Natl. Acad. Sci.* **107**, 21289–21294 (2010).
3. Liu, Y., Cheng, J., Schmid, B. & Sheng, J. Aridity shifts the difference in carbon uptake and storage between wooded and pure grasslands from positive to negative. *Sci. Total Environ.* **861**, 160614 (2023).
4. Shi, H. et al. Terrestrial biodiversity threatened by increasing global aridity velocity under high-level warming. *Proc. Natl. Acad. Sci.* **118**, e2015552118 (2021).
5. Smith, T. & Boers, N. Global vegetation resilience linked to water availability and variability. *Nat. Commun.* **14**, 498 (2023).
6. Maestre, F. T. et al. Structure and Functioning of Dryland Ecosystems in a Changing World. *Annu. Rev. Ecol., Evol., Syst.* **47**, 215–237 (2016).
7. Fu, Q. & Feng, S. Responses of terrestrial aridity to global warming. *J. Geophys. Res.: Atm.***119**, 7863–7875 (2014).
8. Chai, R. et al. Human-caused long-term changes in global aridity. *npj Clim. Atmos. Sci.* **4**, 65 (2021).
9. Lian, X. et al. Multifaceted characteristics of dryland aridity changes in a warming world. *Nat. Rev. Earth Environ.* **2**, 232–250 (2021).
10. Portmann, R. et al. Global forestation and deforestation affect remote climate via adjusted atmosphere and ocean circulation. *Nat. Commun.* **13**, 5569 (2022).
11. Lee, X. et al. Observed increase in local cooling effect of deforestation at higher latitudes. *Nature* **479**, 384–387 (2011).
12. Tang, T. et al. Biophysical Impact of Land-Use and Land-Cover Change on Subgrid Temperature in CMIP6 Models. *J. Hydrometeorol.* **24**, 373–388 (2023).
13. Li, Y. et al. Local cooling and warming effects of forests based on satellite observations. *Nat. Commun.* **6**, 6603 (2015).
14. Eyring, V. et al. Overview of the Coupled Model Intercomparison Project Phase 6 (CMIP6) experimental design and organization. *Geosci. Model Dev.* **9**, 1937–1958 (2016).
15. Lawrence, D. M. et al. The Land Use Model Intercomparison Project (LUMIP) contribution to CMIP6: rationale and experimental design. *Geosci. Model Dev.* **9**, 2973–2998 (2016).
16. Hurtt, G. C. et al. Harmonization of global land use change and management for the period 850–2100 (LUH2) for CMIP6. *Geosci. Model Dev.* **13**, 5425–5464 (2020).
17. Harris, I., Osborn, T. J., Jones, P. & Lister, D. Version 4 of the CRU TS monthly high-resolution gridded multivariate climate dataset. *Sci. Data* **7**, 109 (2020).
18. Allen, R. G., Pereira, L. S., Raes, D. & Smith, M. In *FAO Irrigation and drainage paper 56*. (FAO - Food and Agriculture Organization of the United Nations, Rome, Italy).

## Acknowledgements

T.T. and J-J.C. acknowledge the support from the Chinese Academy of Sciences (Grant E366161601 and E466301601). G.J. acknowledges the support from the Natural Science Foundation of China (42375115), the Basic Research Program of Jiangsu Province (BK20240170), and the Fundamental Research Funds for the Central Universities (2024300330). H-Y.S. acknowledges the support from the Natural Science Foundation of China (42394132) and the National Key Technology R&D Program of China (2022YFC3201802).

## Author contributions

T.T. and G.J. conceived the study. T.T. collected the data, carried out the data analyses and wrote the initial manuscript. All authors contributed to results interpretation and manuscript polishing.

## Competing interests

The authors declare no competing interests.

## Additional information

**Supplementary information** The online version contains supplementary material available at https://doi.org/10.1038/s41612-025-00978-1.

**Correspondence** and requests for materials should be addressed to Tao Tang or Junji Cao.